Monthly Notices
of the
ROYAL ASTRONOMICAL SOCIETY

MNRAS **507,** 1421–1433 (2021)
Advance Access publication 2021 July 22

https://doi.org/10.1093/mnras/stab2101

# Morphology of weak lensing convergence maps

D. Munshi,[1]★ T. Namikawa,[2] J. D. McEwen,[1] T. D. Kitching[1] and F. R. Bouchet[3]

[1]*Mullard Space Science Laboratory, University College London, Holmbury St Mary, Dorking, Surrey RH5 6NT, UK*
[2]*Department of Applied Mathematics and Theoretical Physics, University of Cambridge, Wilberforce Road, Cambridge CB3 OWA, UK*
[3]*Institut d'Astrophysique de Paris, UMR 7095, CNRS and Sorbonne Universit, 98 bis Boulevard Arago, F-75014 Paris, France*

Accepted 2021 July 16. Received 2021 July 11; in original form 2020 October 14

## ABSTRACT

We study the morphology of convergence maps by perturbatively reconstructing their Minkowski functionals (MFs). We present a systematic study using a set of three *generalized* skew spectra as a function of source redshift and smoothing angular scale. These spectra denote the leading-order corrections to the Gaussian MFs in the quasi-linear regime. They can also be used as independent statistics to probe the bispectrum. Using an approach based on pseudo-$S_\ell$s, we show how these spectra will allow the reconstruction of MFs in the presence of an arbitrary mask and inhomogeneous noise in an unbiased way. Our theoretical predictions are based on a recently introduced fitting function to the bispectrum. We compare our results against state-of-the-art numerical simulations and find an excellent agreement. The reconstruction can be carried out in a controlled manner as a function of angular harmonics $\ell$ and source redshift $z_s$, which allows for a greater handle on any possible sources of non-Gaussianity. Our method has the advantage of estimating the topology of convergence maps directly using shear data. We also study weak lensing convergence maps inferred from cosmic microwave background observations, and we find that, though less significant at low redshift, the *post-Born corrections* play an important role in any modelling of the non-Gaussianity of convergence maps at higher redshift. We also study the cross-correlations of estimates from different tomographic bins.

**Key words:** cosmology – methods: analytical, statistical, numerical – weak lensing.

## 1 INTRODUCTION

The recently completed cosmic microwave background (CMB) experiments such as the Planck Surveyors[1] (Planck Collaboration XVI, 2014; Planck Collaboration VI, 2020b) have provided us a standard model of cosmology. However, many of the outstanding questions including, e.g. but not limited to, the nature of dark matter (DM) and dark energy as well as possible modification of general relativity (GR) on cosmological scales (Joyce et al. 2015; Clifton et al. 2016) or the exact nature of neutrino mass hierarchy (Lesgourgues & Pastor 2016) still remain unclear. The significant increase in precision achieved by stage-IV CMB and large-scale structure (LSS) surveys will allow us to answer some of these questions. It is expected that the ongoing weak lensing surveys [Canada–France–Hawaii Telescope[2], Dark Energy Surveys[3] (Abbott et al. 2016), Dark Energy Spectroscopic Instruments,[4] Prime Focus Spectrograph,[5] and Kilo-Degree Survey (Kuijken et al. 2015)] and stage-IV LSS surveys [*Euclid*[6] (Laureijis et al. 2011), Rubin Observatory[7] (Tyson et al. 2003), and *Roman Space Telescope* (National Research Council 2010)] will provide answers to many of the questions that cosmology is facing.

Weak lensing is responsible for the minute shearing, and magnification in the images of the distant galaxies by the intervening LSS allows us to extract information about clustering of the intervening mass distribution in the Universe (Bartelmann & Schneider 2001; Munshi et al. 2008; Kilbinger 2015; Mandelbaum 2018). Weak lensing also leaves its imprints on the observed CMB sky. The weak lensing surveys are complementary to the galaxy surveys such as Baryon Oscillation Spectroscopic Survey[8] (Eisenstein et al. 2015), Extended Baryon Oscillation Spectroscopic Survey (eBOSS Collaboration 2021), or WiggleZ[9] (Abbott et al. 2016) as they provide an unbiased picture of

---

★ E-mail: D.Munshi@ucl.ac.uk

[1] `http://sci.esa.int/planck/`
[2] `http://www.cfht.hawai.edu/Sciences/CFHLS`
[3] `https://www.darkenergysurvey.org/`
[4] `http://desi.lbl.gov`
[5] `http://pfs.ipmu.jp`
[6] `http://sci.esa.int/euclid/`
[7] `http://www.lsst.org/llst home.shtml`
[8] `http://www.sdss3.org/surveys/boss.php`
[9] `http://wigglez.swin.edu.au/`

the underlying DM distribution, whereas the galaxies and other tracers can only provide a biased picture (Desjacques, Jeong & Schmidt 2018).

However, weak lensing observations are sensitive to small scales where clustering is non-linear and non-Gaussian (Bernardeau et al. 2002). Indeed, the statistical estimates of cosmological parameters based on power spectrum analysis are typically degenerate in cosmological parameter, e.g. $\sigma_8$ and $\Omega_{\rm M}$. External data sets, e.g. CMB as well as tomographic or three-dimensional (3D; Castro, Heavens & Kitching 2005) information, are typically used to lift the degeneracy. However, an alternative procedure would be to use high-order statistics of observables that probe the non-linear regime (Munshi, Heavens & Coles 2011; Munshi et al. 2011a, 2015). Even in the absence of any primordial non-Gaussianity, the gravitational clustering induces mode coupling that results in a secondary non-Gaussianity which is more pronounced at the smaller scales where weak lensing surveys are sensitive. Thus, a considerable amount of effort has been invested in understanding the gravity-induced secondary non-Gaussianity from weak lensing surveys. These statistics include the lower order cumulants (Munshi & Jain 2001) and their correlators (Munshi 2000): the multispectra including the skew spectrum (Munshi & Heavens 2010) and kurtosis spectra (Munshi et al. 2011b) as well as the entire Probability Distribution Function (Munshi & Jain 2000) and the statistics of hot and cold spots. The future surveys such as the *Euclid* survey will be particularly interesting in this regard. With its large fraction of sky coverage, it will be able to detect the gravity-induced non-Gaussianity with a very high signal-to-noise (S/N). It is also worth mentioning here that, in addition to breaking the degeneracy in cosmological parameters, the higher order statistics is also important in understanding the covariance of lower order estimators (Barber, Munshi & Valageas 2004; Munshi, Valageas & Barber 2004; Valageas, Munshi & Barber 2005; Valageas, Barber & Munshi 2010).

Topological estimators such as the Minkowski functionals (MFs) are also important diagnostics in this direction as they carry information at all orders. The MFs have been extensively developed as a statistical tool in a cosmological setting for both two-dimensional (2D; projected) and 3D (redshift) surveys. The MFs have analytically known results for a Gaussian random field, making them suitable for studies of non-Gaussianity. Examples of such studies include CMB data (Schmalzing & Górski 1998; Novikov, Schmalzing & Mukhanov 2000; Hikage et al. 2008; Natoli et al. 2010; Ducout et al. 2013; Planck Collaboration 2016b; Planck Collaboration IX, 2020a), LSS (Gott, Mellot & Dickinson 1986; Coles 1988; Gott et al. 1989, 1992; Melott 1990; Moore et al. 1992; Canavezes et al. 1998; Schmalzing & Diaferio 2000; Kerscher et al. 2001; Hikage et al. 2002, 2008 Park et al. 2005; Hikage, Komatsu & Mastubara 2006), weak lensing (Matsubara & Jain 2001; Sato et al. 2001; Taruya et al. 2002; Munshi et al. 2011d), Sunyaev–Zel'dovich maps (Munshi et al. 2011c), 21cm (Gleser et al. 2006), and *N*-body simulations (Schmalzing & Diaferio 2000; Kerscher et al. 2001). Note that this is an incomplete list of references and we have selected a sample of representative papers from the literature. The MFs are spatially defined topological statistics and, by definition, contain statistical information of all orders. This makes them complementary to the polyspectra methods that are defined in Fourier space. It is also possible that the two approaches will be sensitive to different aspects of non-Gaussianity and systematic effects, although in the weakly non-Gaussian limit it has been shown that the MFs reduce to a weighted probe of the bispectrum (Hikage et al. 2006). In addition to providing cosmological information, MFs can also be useful diagnostics of any unknown systematics as well as baryonic contamination which are expected to affect weak lensing observables (Herenois-Deraps et al. 2016).

This paper is organized as follows: The MFs are reviewed in Section 2. Our notations for the weak lensing statistics in projection are described in Section 3. The generalized skew spectra are expressed in terms of the bispectrum in Section 4. The fitting function we use for our reconstruction is described in Section 5. A very brief description of the simulations is provided in Section 6. We discuss the results in Section 7. The conclusions are presented in Section 8.

## 2 MINKOWSKI FUNCTIONALS

The MFs are related to Hadwiger's theorem (Hadwiger 1959) in integral geometry framework which asserts that a set of $d + 1$ functionals can provide all necessary morphological information of a random field in $d$-dimensional space. These functionals are a unique set of morphological estimators that are *motion invariant* and obey properties such as *convex continuity* as well as *additivity*. These properties are important for computing morphological estimators from a pixelized map. The MFs are defined over an excursion set $\Sigma$ for a given threshold $\nu$ and are expressed in terms of weighted curvature integrals.

In 2D, the three MFs are defined and can be expressed using the following notations of Hikage et al. (2008):

$$V_0(\nu) = \int_\Sigma {\rm d}a; \quad V_1(\nu) = \frac{1}{4}\int_{\partial\Sigma} {\rm d}l; \quad V_2(\nu) = \frac{1}{2\pi}\int_{\partial\Sigma} \mathcal{K}{\rm d}l. \tag{1}$$

Following the standard notation in cosmological literature, we use *da* and *dl* to denote the surface area and line elements for an excursion set $\Sigma$ and its boundary $\partial\Sigma$, respectively, that crosses a threshold. The MFs $V_k(\nu)$ correspond to the area of the excursion set $\Sigma$, the length of its boundary $\partial\Sigma$ as well as the integral of curvature $\mathcal{K}$ along its boundary which is also related to the genus $g$ and hence the Euler characteristics $\chi$.

The MFs can be employed to quantify deviations from Gaussianity. At leading order, the MFs can be constructed completely from the knowledge of the bispectrum alone.

The behaviour of the MFs for a random Gaussian field is well known and is given by Tomita's formula (Tomita 1986). The MFs are denoted by $V_k(\nu)(k = 0,\, 1,\, \text{and } 2)$ for a threshold $\nu = \kappa/\sigma_0$, where $\sigma_0^2 = \langle\kappa^2\rangle$ can be decomposed into two different contributions, namely, Gaussian $V_k^{\mathrm{G}}(\nu)$ and perturbative non-Gaussian contribution $\delta V_k(\nu)$:

$$V_k(\nu) = V_k^{\mathrm{G}}(\nu) + \delta V_k(\nu). \tag{2}$$

We are primarily interested in the gravity-induced non-Gaussian contribution, i.e. $\delta V_k(\nu)$ (Hikage et al. 2008),

$$V_k^{\mathrm{G}}(\nu) = A \exp\left(-\frac{\nu^2}{2}\right) H_{k-1}(\nu); \tag{3}$$

$$\delta V_k(\nu) = A \exp\left(-\frac{\nu^2}{2}\right) \left[\delta V_k^{(2)}(\nu)\sigma_0 + \delta V_k^{(3)}(\nu)\sigma_0^2 + \delta V_k^{(4)}(\nu)\sigma_0^3 + \cdots\right], \tag{4}$$

where $H_k(\nu)$ is the Hermite polynomials. Following the notations introduced in Hikage et al. (2008), we have separated out a normalization factor $A$ in these expressions which is given by the generalized variance parameter $\sigma_0^2$ and $\sigma_1^2$:

$$A = \frac{1}{(2\pi)^{(k+1)/2}} \frac{\omega_2}{\omega_{2-k}\omega_k} \left(\frac{\sigma_1}{\sqrt{2}\sigma_0}\right)^k. \tag{5}$$

Here, $\omega_k = \pi^{k/2}/\Gamma(k/2+1)$ is the volume of a $k$-dimensional unit ball. For projected weak lensing convergence maps in 2D, we only need $\omega_0 = 1$, $\omega_1 = 2$, and $\omega_2 = \pi$. The coefficient depends only on the power spectrum of the perturbation through $\sigma_0$ and $\sigma_1$. These quantities are defined through the following expression:

$$\sigma_j^2 = \frac{1}{2\pi} \sum_\ell [\ell(\ell+1)]^j (2l+1) \mathcal{C}_\ell W_\ell^2. \tag{6}$$

Here, $\mathcal{C}_\ell$ is the angular power spectrum of the underlying field and $W_\ell$ is the window function used to smooth a map. A more through discussion will be presented in the following section for $\kappa$ maps. At the level of the bispectrum, the perturbative corrections are determined by three generalized skewness paramters $S^{(k)}$ (Hikage et al. 2008):

$$\delta V_k^{(2)}(\nu) = \left[\left\{\frac{1}{6} S^{(0)} H_{k+2}(\nu) + \frac{k}{3} S^{(1)} H_k(\nu) + \frac{k(k-1)}{6} S^{(2)} H_{k-2}(\nu)\right\}\right]. \tag{7}$$

The skewness parameters can also be expressed as (Munshi et al. 2011d):

$$S^{(0)} = \frac{\langle\kappa^3\rangle}{\sigma_0^2}; \quad S^{(1)} = \frac{\langle\kappa^2\nabla^2\kappa\rangle}{\sigma_0^2\sigma_1^2}; \quad S^{(2)} \equiv \frac{\langle|\nabla\kappa|^2\nabla^2\kappa\rangle}{\sigma_1^2}. \tag{8}$$

Here, $S^{(0)}$ is the ordinary skewness parameter, whereas $S^{(1)}$ and $S^{(2)}$ are its higher order generalizations. At next order, a set of four kurtosis parameters can be used to express the next-order correlations (Munshi et al. 2011d). The primary motivation of this article is to reconstruct these generalized skewness parameters using spectra associated with them, which allows us to estimate them from surveys in the presence of complicated mask and noise. We will borrow the analytical tools developed in Munshi et al. (2011d).

## 3 WEAK LENSING POWER SPECTRUM AND BISPECTRUM

The weak lensing convergence denoted as $\kappa$ can be expressed in terms of a line-of-sight (los) integration of 3D density contrast $\delta$:

$$\kappa(\boldsymbol{\theta}, r_{\mathrm{s}}) = \int_o^{r_{\mathrm{s}}} \mathrm{d}r\, \omega(r, r_{\mathrm{s}})\delta(\boldsymbol{\theta}, r); \quad \omega(r, r_{\mathrm{s}}) = \frac{3}{2\,a}\frac{H_0^2}{c^2}\Omega_{\mathrm{M}}\frac{d_{\mathrm{A}}(r-r_{\mathrm{s}})}{d_{\mathrm{A}}(r)d_{\mathrm{A}}(r_{\mathrm{s}})}. \tag{9}$$

In our notation, $r = |\boldsymbol{r}|$ denotes the *comoving* radial distance to the source and $\boldsymbol{\theta}$ denotes the angular position on the sky. The background cosmology is specified in terms of $\Omega_{\mathrm{M}}$ which denotes the cosmological matter density parameter (that describes the total matter density in units of the critical density), and $H_0$ which denotes the Hubble constant; $c$ is the speed of light and $a = 1/(1+z)$ denotes the scale factor at a redshift $z$. The comoving angular diameter distance at a comoving radial distance $r$ is represented as $d_{\mathrm{A}}(r)$. The source plane is assumed to be at a redshift $z_{\mathrm{s}}$, or equivalently at comoving radial distance $r_{\mathrm{s}}$. To simplify the analysis, we will ignore source distribution and photometric redshift errors. We will focus on the morphological estimators as a function of $z_{\mathrm{s}}$.

For the smoothed convergence $\kappa$, the mean is 0, $\langle\kappa(\boldsymbol{\theta})\rangle = 0$, and using a spherical harmonic decomposition of $\kappa(\boldsymbol{\theta})$, using spherical harmonics $Y_{\ell m}(\boldsymbol{\theta})$ as the basis functions, $\kappa(\boldsymbol{\theta}) = \sum_{\ell m} \kappa_{\ell m} Y_{\ell m}(\boldsymbol{\theta})$, we can define its angular power spectrum $\mathcal{C}_l$ in terms of the harmonic coefficients $\kappa_{\ell m}\langle\kappa_{\ell m}\kappa^*_{\ell' m'}\rangle = \mathcal{C}_\ell \delta_{\ell\ell'}\delta_{mm'}$ , which is a sufficient statistical characterization of a Gaussian field.

$$\mathcal{C}_\ell = \int_0^{r_{\mathrm{s}}} \mathrm{d}r \frac{w^2(r, r_{\mathrm{s}})}{d_{\mathrm{A}}^2(r)} P\left(\frac{\ell}{d_{\mathrm{A}}(r)}; r\right). \tag{10}$$

The convergence bispectrum $\mathcal{B}$ can likewise be expressed using the following los integration of the bispectrum of the density contrast $\delta$ denoted as $B_\delta$ (see Munshi et al. 2008):

$$\langle\kappa_{\ell_1 m_1}\kappa_{\ell_2 m_2}\kappa_{\ell_3 m_3}\rangle_c \equiv \mathcal{B}_{\ell_1\ell_2\ell_3}\begin{pmatrix}\ell_1 & \ell_2 & \ell_3\\ m_1 & m_2 & m_3\end{pmatrix}. \tag{11}$$

The matrix above represents a Wigner 3$j$-symbol and the angular brackets here represent ensemble averaging. This particular form is employed as it preserves the rotational invariance of the three-point correlation function.

The Wigner 3*j*-symbol is non-zero only when the triplets ($\ell_1$, $\ell_2$, and $\ell_3$) satisfy the *triangularity* condition $|\ell_1 - \ell_2| \le \ell_3 \le \ell_1 + \ell_2$ as well as the condition that the sum $\ell_1 + \ell_2 + \ell_3$ is even. This ensures the parity invariance of the bispectrum and neglects the presence of any parity violating physics. This selection rule is imposed by the invariance of the field under spatial inversion. Indeed, the parity violating contributions at the level of the bispectrum can be obtained by including both the (so-called) Electric (E) and Magnetic (B) modes (Munshi et al. 2011a). This can be used to detect any possible parity violating physics as well as other systematic effects.

The convergence bispectrum $\mathcal{B}$ is expressed in terms of the bispectrum for the density contrast: $B$:

$$\mathcal{B}_{\ell_1\ell_2\ell_3} = I_{\ell_1\ell_2\ell_3}\int_0^{r_s} \mathrm{d}r\, \frac{w^3(r, r_\mathrm{s})}{d_\mathrm{A}^4(r)} B\left(\frac{\ell_1}{d_\mathrm{A}(r)}, \frac{\ell_2}{d_\mathrm{A}(r)}, \frac{\ell_3}{d_\mathrm{A}(r)}; r\right); \tag{12}$$

$$I_{\ell_1\ell_2\ell_3} = \sqrt{\frac{(2\ell_1+1)(2\ell_2+1)(2\ell_3+1)}{4\pi}} \begin{pmatrix} \ell_1 & \ell_2 & \ell_3 \\ 0 & 0 & 0 \end{pmatrix}. \tag{13}$$

The cross-spectrum $\mathcal{C}_\ell^{\alpha\beta}$ and mixed bispectrum $\mathcal{B}^{\alpha\beta}_{\ell_1\ell_2\ell_3}$ involving two topographic bins $\alpha$ and $\beta$ have the following form:

$$\mathcal{C}_\ell^{\alpha\beta} = \int_0^{r_\mathrm{min}} \mathrm{d}r\, \frac{\omega_\alpha(r)\omega_\beta(r)}{d_\mathrm{A}^2(r)} P\left(\frac{l}{d_\mathrm{A}(r)}; r\right); \tag{14a}$$

$$\mathcal{B}^{\alpha\beta}_{\ell_1\ell_2\ell_3} = I_{\ell_1\ell_2\ell_3}\int_0^{r_\mathrm{min}} \mathrm{d}r\, \frac{\omega^1_\alpha(r)\omega^2_\beta(r)}{d_\mathrm{A}^4(r)} B\left(\frac{\ell_1}{d_\mathrm{A}(r)}, \frac{\ell_2}{d_\mathrm{A}(r),}, \frac{\ell_3}{d_\mathrm{A}(r)}; r\right); \quad r_\mathrm{min} = \min(r_\alpha, r_\beta); \tag{14b}$$

$$w_i(r) := \frac{3\Omega_\mathrm{M}}{2}\frac{H_0^2}{c^2} a^{-1} \frac{d_\mathrm{A}(r) d_\mathrm{A}(r_\mathrm{si} - r)}{d_\mathrm{A}(r_\mathrm{si})}; \quad i \in \{\alpha, \beta\}. \tag{14c}$$

Using these expressions (derived using Limber approximation), we will next construct the generalized skew spectra that are useful in constructing the MFs.

## 4 GENERALIZED SKEW SPECTRA

Individual triplets of harmonics ($\ell_1$, $\ell_2$, and $\ell_3$) define a triangle in the harmonic domain and specify a bispectral mode. The skew spectra defined below are summed over all possible configurations of the bispectrum by keeping one side of the triangle fixed. Following Munshi et al. (2011d), we introduce the generalized skew spectra $S_\ell^{(i)}$:

$$S_\ell^{(0)} = \frac{1}{12\pi\sigma_0^4}\frac{1}{2\ell+1}\sum_m \mathrm{Real}\left\{\left[\kappa^2\right]_{\ell m}[\kappa]^*_{\ell m}\right\} = \frac{1}{12\pi\sigma_0^4}\sum_{\ell_1\ell_2} \mathcal{B}_{\ell\ell_1\ell_2} J_{\ell\ell_1\ell_2} W_\ell W_{\ell_1} W_{\ell_2}; \tag{15a}$$

$$S_\ell^{(1)} = \frac{1}{16\pi\sigma_0^2\sigma_1^2}\frac{1}{2\ell+1}\sum_m \mathrm{Real}\{[\kappa^2]_{\ell m}\nabla^2[\kappa]^*_{\ell m}\} = \frac{1}{16\pi\sigma_0^2\sigma_1^2}\ell(\ell+1)\sum_{\ell_i} \mathcal{B}_{\ell\ell_1\ell_2} J_{\ell\ell_1\ell_2} W_\ell W_{\ell_1} W_{\ell_2}; \tag{15b}$$

$$\begin{aligned} S_\ell^{(2)} &= \frac{1}{8\pi\sigma_1^4}\frac{1}{2\ell+1}\sum_m \mathrm{Real}\{[\nabla\kappa\cdot\nabla\kappa]_{\ell m}[\kappa^2]^*_{\ell m}\} \\ &= \frac{1}{8\pi\sigma_1^4}\sum_{\ell_i}\Big[[\ell(\ell+1) + \ell_1(\ell_1+1) - \ell_2(\ell_2+1)]\ell_2(\ell_2+1)\Big] \mathcal{B}_{\ell\ell_1\ell_2} J_{\ell\ell_1\ell_2} W_\ell W_{\ell_1} W_{\ell_2}. \end{aligned} \tag{15c}$$

We have introduced the following notations above:

$$J_{\ell_1\ell_2\ell_3} \equiv \frac{I_{\ell_1\ell_2\ell_3}}{2\ell_3+1} = \sqrt{\frac{(2\ell_1+1)(2\ell_2+1)}{(2\ell_3+1)4\pi}} \begin{pmatrix} \ell_1 & \ell_2 & \ell_3 \\ 0 & 0 & 0 \end{pmatrix}; \tag{15d}$$

$$W_\ell = \exp\left[-\ell(\ell+1)\frac{\theta_s^2}{8\ln 2}\right]. \tag{15e}$$

We will study these spectra using numerical simulations and test them against theoretical predictions that rely on a fitting function-based approach. We will use a Gaussian window function $W_\ell$ in our study but the expressions are valid for arbitrary window function, including the top-hat or compensated window (filter) functions. The one-point skewness parameters $S^{(i)}$ can be recovered from their respective skew spectra, which were used in equation (8):

$$S^{(i)} = \frac{1}{4\pi}\sum_l (2\ell+1) S_\ell^{(i)}. \tag{16}$$

Expressions for the skew spectra in equations (15a–15c) can also be generalized to include cases where instead of individual bins two different bins are cross-correlated.

$$S_\ell^{(0)\alpha\beta} = \frac{1}{2\ell+1}\sum_m \mathrm{Real}\{[\kappa_\alpha^2]_{\ell m}[\kappa_\beta]^*_{\ell m}\} = \frac{1}{12\pi\sigma_0^4}\sum_{\ell_1\ell_2} \mathcal{B}^{\alpha\beta}_{\ell\ell_1\ell_2} J_{\ell\ell_1\ell_2} W_\ell W_{\ell_1} W_{\ell_2}. \tag{17}$$

Similar expressions can be obtained for the other skew spectra by replacing $\mathcal{B}_{\ell\ell_1\ell_2}$ by $\mathcal{B}^{\alpha\beta}_{\ell\ell_1\ell_2}$ in equations (15b–15c). The mixed bispectra $\mathcal{B}^{\alpha\beta}_{\ell\ell_1\ell_2}$ is defined in equation (14b). Notice that by construction $S_\ell^{(i)\alpha\beta} \ne S_\ell^{(i)\beta\alpha}$ as $\mathcal{B}^{\alpha\beta}_{\ell\ell_1\ell_2} \ne \mathcal{B}^{\beta\alpha}_{\ell\ell_1\ell_2}$.

Although we have adopted an harmonic approach, equivalent information about the non-Gaussianity can also be obtained by studying the corresponding *collapsed* three-point correlation functions. This approach will be more efficient for surveys with smaller sky coverage and in the presence of a non-trivial mask:

$$S^{(0)\alpha\beta}_{12}(\theta)=\langle\kappa^2_\alpha(\boldsymbol{\theta}_1)\kappa_\beta(\boldsymbol{\theta}_2)\rangle;\quad S^{(1)\alpha\beta}_{12}(\theta)=\langle\kappa^2_\alpha(\boldsymbol{\theta}_1)\nabla^2\kappa_\beta(\boldsymbol{\theta}_2)\rangle;\quad S^{(2)\alpha\beta}_{12}(\theta)=\langle\nabla^2\kappa_\alpha(\boldsymbol{\theta}_1)[\nabla\kappa_\beta(\boldsymbol{\theta}_2)\cdot\nabla\kappa_\beta(\boldsymbol{\theta}_2)]\rangle; \tag{18}$$

Due to the isotropy and homogeneity of the background Universe, these correlation functions are only a function of the separation angle $\theta=|\boldsymbol{\theta}_1-\boldsymbol{\theta}_2|$. These two-point correlations can be constructed by cross-correlating derived maps from different topographic bins $\kappa^2_\alpha(\boldsymbol{\theta})$, $\nabla^2\kappa_\alpha(\boldsymbol{\theta})$, and $\nabla\kappa_\alpha(\boldsymbol{\theta})\cdot\nabla\kappa_\alpha(\boldsymbol{\theta})$. In terms of the skew spectra, these correlation functions can be expressed as

$$S^{(i)\alpha\beta}_{12}(\theta)=\frac{1}{4\pi}\sum_\ell(2\ell+1)P_\ell(\cos\theta)S^{(i)}_\ell;\qquad i\in\{0,1,2\}. \tag{19}$$

Here, $P_\ell$ denotes the Legendre polynomial of order $\ell$.

So far, we have assumed a full sky coverage for the estimation of the generalized skew spectra. However, most surveys will have a partial sky coverage. The pseudo-skew spectrum (PSL) technique presented in Munshi et al. (2020a) is also valid for the generalized skew spectra. An unbiased all-sky estimate $\hat{S}_\ell$ can be constructed from the masked skew spectra $\tilde{S}_\ell$ using the expression below:

$$\tilde{S}^{(i)}_\ell=M_{\ell\ell'}S^{(i)}_{\ell'};\quad \hat{S}^{(i)}_\ell=M^{-1}_{\ell\ell'}\tilde{S}^{(i)}_{\ell'}; \tag{20a}$$

$$\langle\hat{S}^{(i)}_\ell\rangle=S^{(i)}_\ell, \tag{20b}$$

where the mode-coupling (mixing) matrix is given by

$$M_{\ell\ell'}=(2\ell'+1)\sum_{\ell''}\begin{pmatrix}\ell & \ell' & \ell''\\ 0 & 0 & 0\end{pmatrix}^2\frac{(2\ell''+1)}{4\pi}|w^2_{\ell''}|. \tag{21}$$

Here, we have introduced the power spectrum of the mask $w(\boldsymbol{\theta})$, i.e. $w_\ell=1/(2\ell+1)\sum_m|w_{\ell m}|^2$, constructed from the harmonic coefficient $w_{\ell m}$ and its complex conjugate $w^*_{\ell m}$ (see Munshi et al. 2020a, for more detailed discussion). Notice that a (inhomogeneous) Gaussian noise does not contribute to the generalized skew spectra though it will increase the scatter. This PSL method will be essential for constructing MFs of weak lensing $\kappa$ maps in the presence of a mask with a non-trivial topology. For a small sky coverage, the matrix $M_{\ell\ell'}$ may not be invertible and a binning may be necessary.

## 5 FITTING FUNCTION FOR BISPECTRUM

In second-order Eulerian perturbation theory, the matter bispectrum $B(\mathbf{k}_1,\mathbf{k}_2$, and $\mathbf{k}_3)$ that encodes mode coupling of the 3D density contrast in the Fourier domain can be expressed as (Bernardeau et al. 2002)

$$B(k_1,k_2,k_3)=2F_2(k_1,k_2)P_{lin}(k_1)P_{lin}(k_2)+\text{cyc.perm..} \tag{22a}$$

Here, $F_2$ is the kernel that encapsulates the second-order mode–mode coupling and $P_{lin}(k)$ denotes the linear power spectrum of the density contrast $\delta$. In a fitting function approach, the analytical form of the kernel $F_2$ is generalized from the quasi-linear regime to non-linear regime by introducing three independent coefficients $a(n_\mathrm{e},k)$, $b(n_\mathrm{e},k)$, and $c(n_\mathrm{e},k)$ that are determined using numerical simulations.

$$F_2(k_1,k_2)=\frac{5}{7}a(n_\mathrm{e},k)a(n_\mathrm{e},k)+\frac{1}{2}\left(\frac{k_1\cdot k_2}{k_2^2}+\frac{k_1\cdot k_2}{k_1^2}\right)b(n_\mathrm{e},k)b(n_\mathrm{e},k)+\frac{2}{7}\left(\frac{k_1\cdot k_2}{k_1k_2}\right)^2c(n_\mathrm{e},k)c(n_\mathrm{e},k). \tag{22b}$$

Here, $n_\mathrm{e}$ is local logarithmic slope of the power spectrum at 3D wavenumber $k$. In the quasi-linear regime, these coefficients approach unity, i.e. $a=b=c=1$. In the highly non-linear regime, if we set $a\neq 0$ and $b=c=0$, we recover the hierarchal form for the matter bispectrum. The idea of a fitting function was initially proposed by Scoccimarro & Frieman (1999). It interpolates between the perturbative and non-linear regimes. It has a limited validity range of $k<3\,h\,\mathrm{Mpc}^{-1}$ and $z\approx 0$–1. The functional form of this fitting function was later improved by Gil-Marin et al. (2012) with a rather limited validity range of $k<0.4\,h\,\mathrm{Mpc}^{-1}$ and $z\approx 1.5$. The improvement was achieved by introducing additional free parameters which are extracted from numerical simulations. The inaccuracy of this fitting function was pointed out by Munshi et al. (2020b). An even more accurate fitting function was recently proposed by Takahashi et al. (2017). This new fitting function has a validity range of $k<10\,h\,\mathrm{Mpc}^{-1}$ and $z\approx 1$–3. Its higher accuracy is important for a very accurate theoretical prediction of secondary non-Gaussianity across the range of wavelength and redshift that will be useful for stage-IV LSS experiments including *Euclid*. This function has already been used by Munshi et al. (2020a). In our study, we will use it to compute the theoretical predictions for our morphological estimators.

For modelling of skew spectrum related to secondary non-Gaussianity, using halo model (HM) as well as primordial non-Gaussianity, see Munshi et al. (2011d).

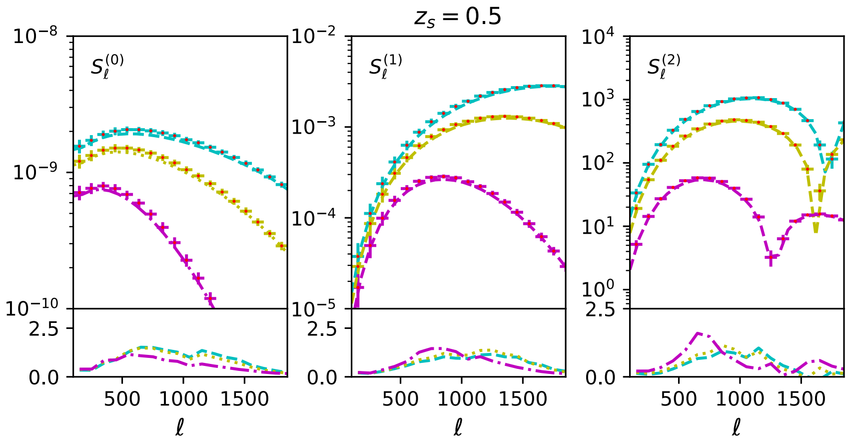

**Figure 1.** From left to right, different panels depict the skew spectra $S^0_\ell$, $S^{(1)}_\ell$, and $S^{(1)}_\ell$, respectively, as a function of $\ell$. The data points with error bars in each panel are the bin-averaged values of the respective skew spectra estimated from simulations. Different curves in each panel correspond to different smoothing angular scales. These generalized skew spectra are defined in equations (15a–15c). In each panel, three different smoothing angular scales $\theta_s = 2$, 5, and 10 arcmin (from top to bottom) are shown. The source redshift is fixed at $z_s = 0.5$. A Gaussian smoothing window was used. See the text for more details. The bottom subpanels for each panel show the deviation $\Delta_l$ of simulations $S^{\rm sim}_\ell$ from theoretical prediction $S^{\rm th}_\ell$ in units of standard deviation $\sigma_\ell$ computed for individual beans, i.e. $\Delta_\ell = (S^{\rm th}_\ell - S^{\rm sim}_\ell)/\sigma_\ell$. No noise or mask was used. For $S^2_\ell$, the absolute value $|S^2_\ell|$ is shown in the third panel; the dip feature in this case signifies a zero crossing.

## 6 SIMULATIONS

In our numerical investigations, we use the all-sky weak lensing maps described in Takahashi et al. (2017).[10] These maps were generated using ray tracing through $N$-body simulations using multiple lens planes and to generate convergence $\kappa$ as well as shear $\gamma$ maps. They do not employ the Born approximation. The post-Born corrections are known to play an important role at higher redshifts especially for CMB lensing. The source redshifts used were in the range $z_s = 0.05{-}5.30$ at an interval of $\Delta z_s = 0.05$. We have used the maps corresponding to source redshifts of $z_s = 0.5$, 1.0, 1.5, and 2.0 in our study. For generating lensed CMB maps, numerical simulations were replaced by Gaussian realizations of density fluctuations in the redshift range $z_s = 7.1{-}1100.0$. The perturbations were generated using a linear matter power spectrum. These maps were generated using different resolution in `HEALPix`[11] format (Gorski et al. 2016) using an equal area pixelization scheme. The number of pixels scales as $N_{\rm pix} = 12N^2_{\rm side}$ with the resolution parameter $N_{\rm side}$. We will be using maps generated at a resolution $N_{\rm side} = 4096$ and used maps at a higher resolution for various sanity checks. In our study, we will be restricting us to $\ell \le \ell_{\rm max}$ with $\ell_{\rm max} = 2000$. However, the $\ell_{\rm max}$ is kept flexible in our analytical formalism and can be used to filter out any astrophysical complexities related to baryonic feedback (Weiss et al. 2019).

The cosmological parameters used are $\Omega_{\rm CDM} = 0.233$, $\Omega_{\rm b} = 0.046$, $\Omega_{\rm M} = \Omega_{\rm CDM} + \Omega_{\rm b}$, $\Omega_\lambda = 1 - \Omega_{\rm M}$, and $h = 0.7$, where CDM denotes cold dark matter. For the amplitude of density fluctuation, $\sigma_8 = 0.82$, and the spectral index $n_s = 0.97$ is used. These maps were recently used to analyse the bispectrum in the context of CMB lensing (Namikawa et al. 2019) as well in studies of lensing-induced bispectrum at a low redshift (Munshi et al. 2020a, b).

## 7 RESULTS AND DISCUSSION

In this section, we will summarize the main results presented in this paper along with their implications.

(i) *Skew spectra for individual tomographic bins at a low redshift:* In Figs 1–4, the generalized skew spectra $S^{(0)}_\ell$, $S^{(1)}_\ell$, and $S^{(2)}_\ell$ (from left to right) are being plotted as a function of $\ell$. These figures correspond to different source redshifts $z_s = 0.5$, 1.0, 1.5, and 2.0, respectively. The various line styles in each panel correspond to different smoothing angular scales. We use a Gaussian window in our study. From top to bottom, different curves represent full width at half-maximum of $\theta_s = 2.0$, 5.0, and 10.0 arcmin, respectively. We use the noise free simulations described in Section 6. We have used equations (15a–15c) to evaluate the theoretical expectations for $S^{(0)}_\ell$, $S^{(1)}_\ell$, and $S^{(2)}_\ell$ along with the fitting function by Takahashi et al. (2017) discussed in Section 5. We have used theoretical predictions with and without the post-Born approximation but we find that inclusion of such corrections makes no significant impact on theoretical predictions. Over the entire range of smoothing angular scales $\theta_s$ and angular harmonics $\ell$ studied, we have not found any significant departure from theoretical predictions. We have used $N_{\rm side} = 4096$ in our study. The skew spectra are sensitive to the $\ell_{\rm max}$. We have included all modes up to $\ell_{\rm max} = 2000$ in our calculation in our theoretical predictions. To be consistent, we have also filtered all modes higher than $\ell_{\rm max}$ while processing the numerical simulations. We have also tested the impact of retaining the lower harmonics in our numerical evaluation by filtering out these modes from the maps as well as keeping them

---

[10] http://cosmo.phys.hirosaki-u.ac.jp/takahasi/allsky_raytracing/

[11] https://healpix.jpl.nasa.gov/

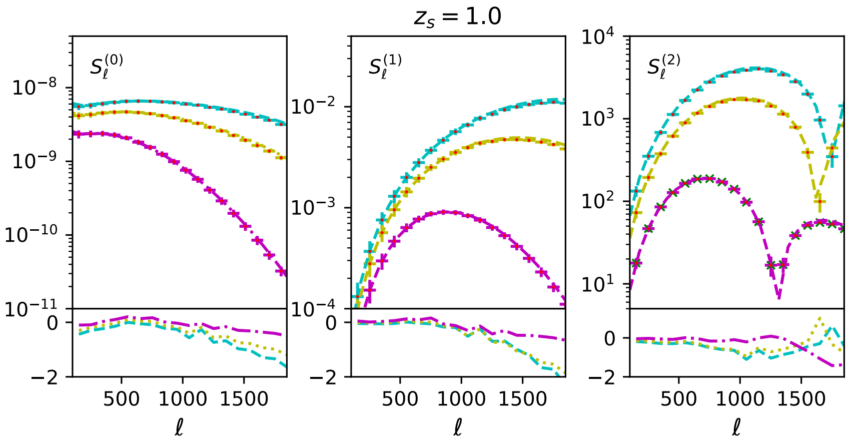

**Figure 2.** Same as Fig. 1, but for $z_s = 1.0$.

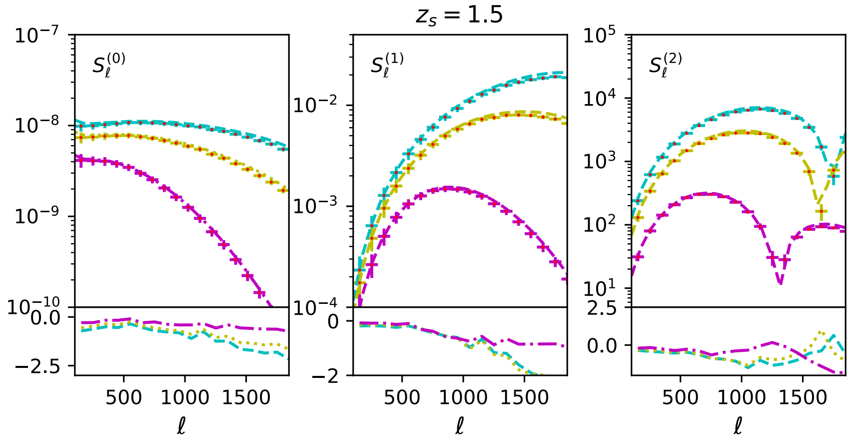

**Figure 3.** Same as Fig. 1, but for $z_s = 1.5$.

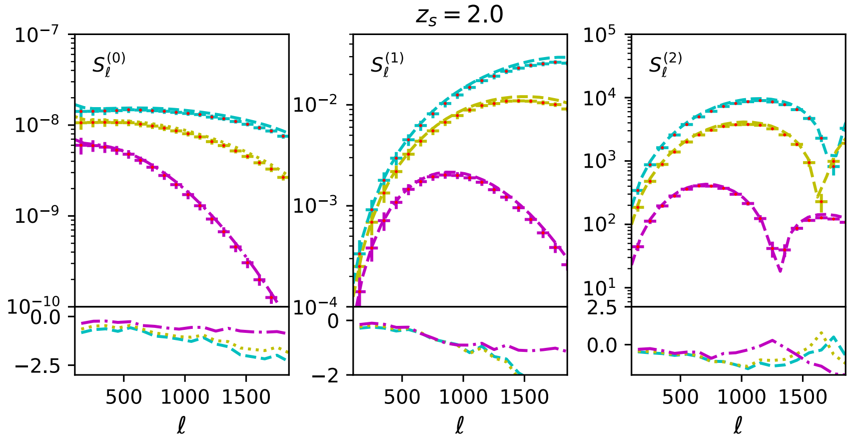

**Figure 4.** Same as Fig. 1, but for $z_s = 2.0$.

in while computing the skew-$S_\ell$s. We did not find any statistically significant difference in our final results. The flexibility and simplicity with which the skew spectra can be evaluated give a very efficient method to study the spectra in a mode-by-mode manner, thus providing a greater handle on dealing with any possible systematics. Notice that the perturbative reconstruction of the MFs requires the expansion parameter $\sigma_0$ introduced in equation (4) to be small for the series to be convergent, but the three skew spectra can also be used as independent estimators of non-Gaussianity and a method of effective data compression in their own right. This makes them attractive even when the series in equation (7) is divergent at smaller angular scales. The convergence of the series expansion and its implications were considered in Petri et al. (2013) to some extent. However, a detailed study is needed for a realistic assessment as a function of various survey parameters.

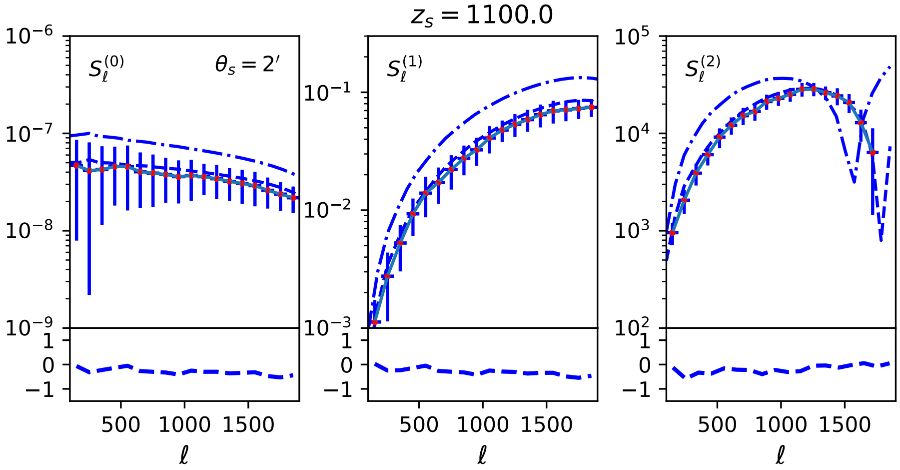

**Figure 5.** The generalized skew spectra for $\kappa$ maps are shown for $z_s = 1100$. From left to right, we show results for the skew spectra $S_\ell^{(0)}$, $S_\ell^{(1)}$, and $S_\ell^{(2)}$ as a function of $\ell$. These generalized skew spectra are defined in equations (15a–15c). The $\kappa$ maps are inferred from CMB temperature maps. The dot–dashed and dashed lines represent the theoretical predictions based on Born and post-Born approximations, respectively. The importance of post-Born approximation is more pronounced at higher redshift. The smoothing angular scale is fixed at $\theta_s = 2$ arcmin. Results are obtained using one all-sky map. No noise was included. An all sky coverage was assumed. The error bars were computed using the scatter within the bin fixed at $\delta\ell = 100$.

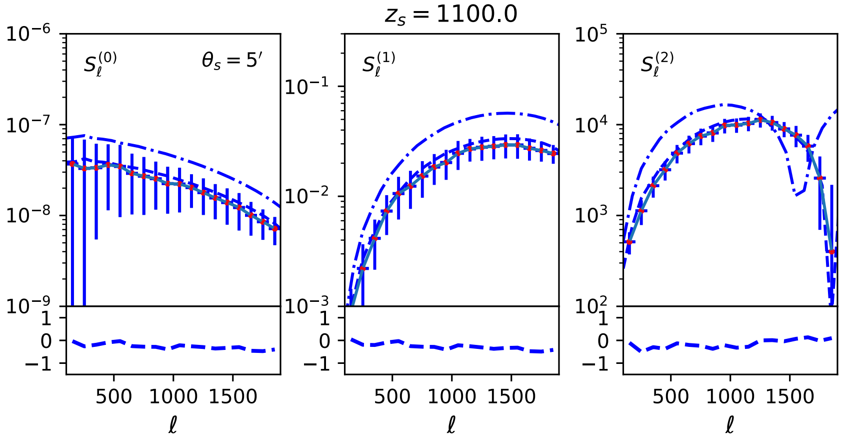

**Figure 6.** Same as Fig. 5, but for $\theta_s = 5.0$ arcmin.

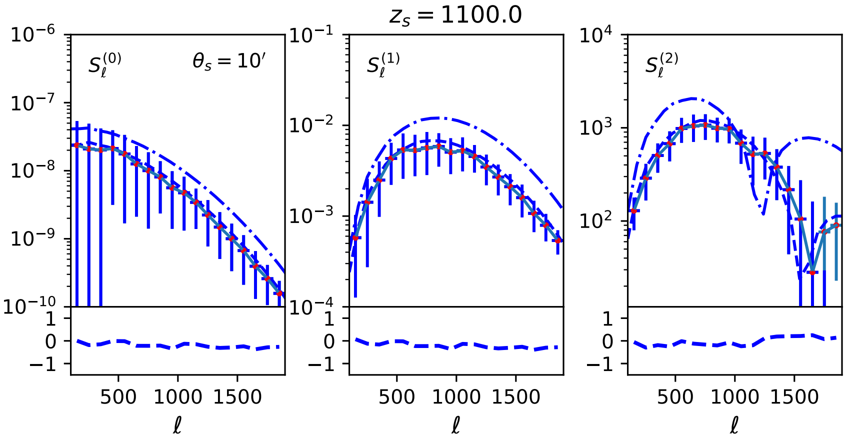

**Figure 7.** Same as Fig. 5, but for $\theta_s = 10.0$ arcmin.

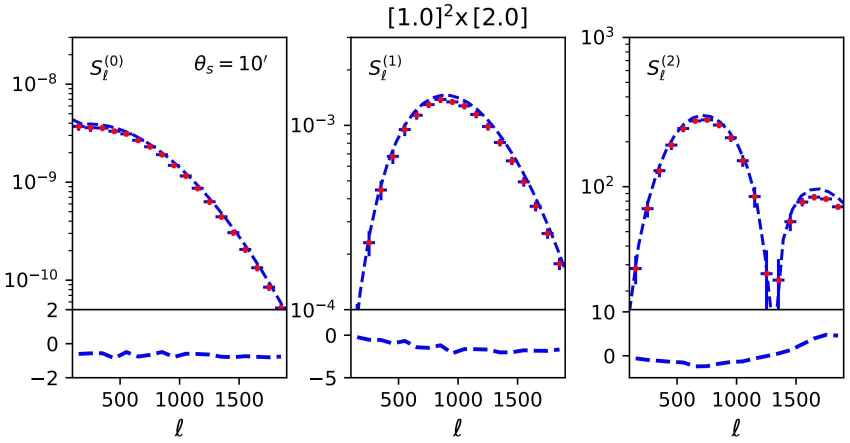

**Figure 8.** We have chosen two redshift bins $z_1 = 1.0$ and $z_2 = 2.0$. From left to right, we show results for the skew spectra $S_\ell^{(0)}$, $S_\ell^{(1)}$, and $S_\ell^{(2)}$ as a function of $\ell$. The smooth curves represent theoretical predictions, whereas data points represent estimates from the simulations. These generalized skew spectra are defined in equations (15a–15c). In each panel, we show $\langle\kappa_1^2\kappa_2\rangle$ [in our notation, $\kappa_1 = \kappa(z_1)$) and $\kappa_2 = \kappa(z_2)$] and $\langle\kappa_1^2\kappa_2\rangle$ for two different smoothing angular scales $\theta_s =$ 10 arcmin. One single all-sky map was used to construct the skew spectra. No noise was included in our study.

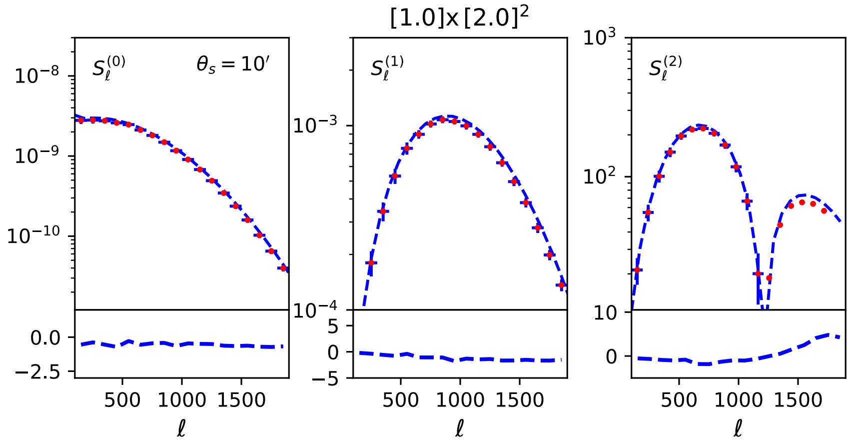

**Figure 9.** Same as Fig. 8 but the skew spectra associated with $\langle\kappa_1\kappa_2^2\rangle$ are being plotted.

(ii) *Skew spectra from CMB maps:* In Figs 5–7, the generalized spectra $S^{(0)}$ (left-hand panel), $S^{(1)}$ (middle panel), and $S^{(2)}$ (right-hand panel) are plotted for redshift $z_s = 1100.0$. The convergence maps are inferred from CMB observations. The variance or skew spectra increases with redshift or the depth of the survey. To reduce the scatter in our estimates, we have used binning with a bin size $\Delta_\ell = 100$. While in Fig. 5 the smoothing angular scale is sized at $\theta_s = 2$ arcmin, in Figs 6 and 7 this angular scale is fixed, respectively, at $\theta_s = 5$ and 10 arcmin. The dot–dashed lines correspond to Born approximation. The dot–dashed lines in each panel include the post-Born corrections. The important difference of the CMB skew spectra with the ones at lower redshifts is the significance of post-Born correction in modelling of non-Gaussianity. The post-Born correction is non-linear and it is known to generate a non-negligible bispectrum of the convergence (Marozzi et al. 2016; Pratten & Lewis 2016). Our study confirms that the post-Born contributions to the bispectrum can significantly change the shape predicted for the skew spectrum from the LSS non-linearities alone. This is more obvious in the right-hand panels where the generalized skew spectrum $S_\ell^{(2)}$ changes a signature from positive at lower $\ell$ to negative at higher $\ell$.

(iii) *Skew spectrum from cross-correlating two different tomographic bins:* In addition to studying the skew spectra from individual tomographic bins, we have also cross-correlated different bins to construct the skew spectra. Indeed, the link to morphology no longer exists but this gives us a clue about how these estimators are correlated. It can also be argued, irrespective of morphological connection, that these estimators provide a tool for data compression that is simple to implement.

In Figs 8 and 9, we show the cross-skew spectra of two tomographic bins, $z_s = 1.0$ and 2.0. We have fixed $\theta_s = 10$ arcmin in each of these plots. The error bars are computed using the fluctuations within a bin. The bin size is $\Delta_\ell = 100$. In each case, we find that the analytical and numerical predictions agree within $2\sigma$ in the cosmic variance limited case. In Figs 10 and 11, we plot the skew spectra constructed from $\kappa$ maps inferred from CMB observations at $z_s = 1100$ (denoted as $\kappa_{\rm LSS}$) and cross-correlated against convergence map at $z_s = 1.0$ (denoted as $\kappa_1$).

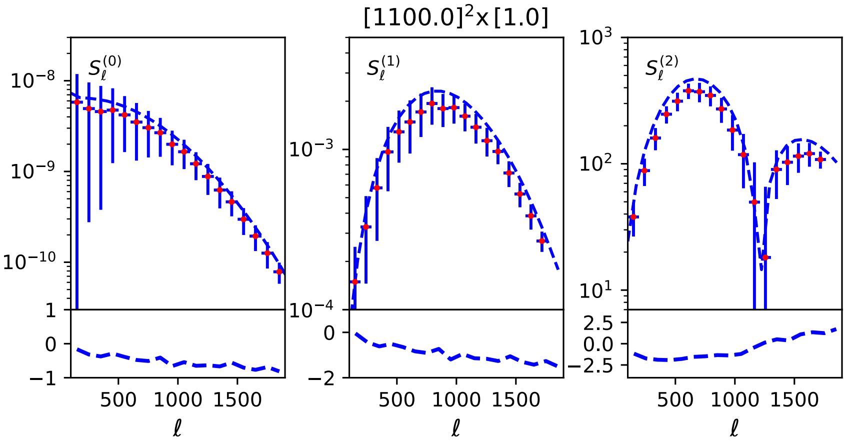

**Figure 10.** Same as Fig. 8 but for $z_1 = 1100$ and $z_2 = 1.0$. For $z_s = 1100$, the $\kappa$ is being inferred from CMB observations.

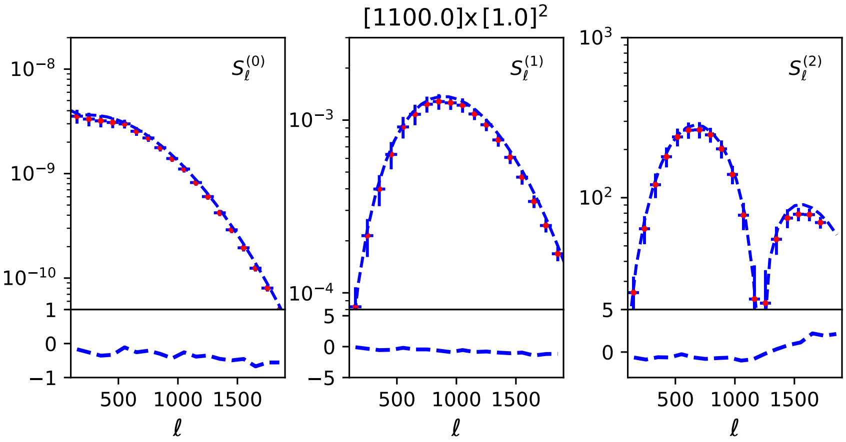

**Figure 11.** Same as Fig. 10 but for $z_1 = 1.0$ and $z_2 = 1100.0$.

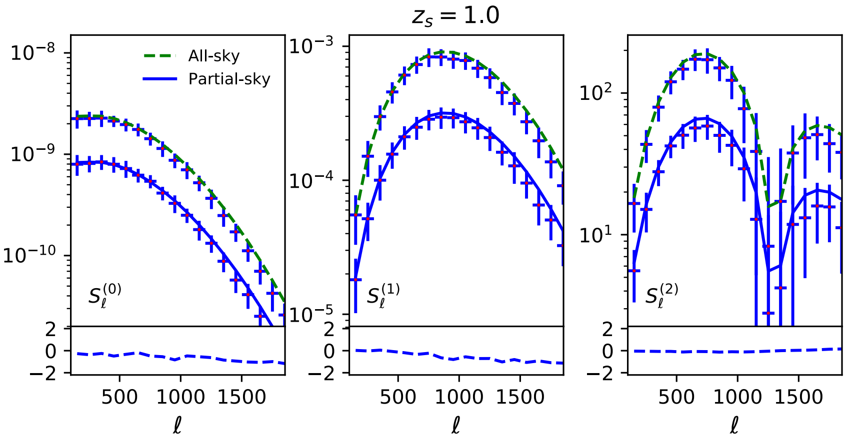

**Figure 12.** We show the three skew spectra for a *Euclid*-like survey. In our study, we use a 'pseudo *Euclid*'' mask. All pixels lying within 22 deg of either the galactic or ecliptic planes are discarded while constructing the mask, which leaves 14 490 deg$^2$ of the sky-making fraction of the sky covered $f_{\rm sky} \approx 0.35$ (see Munshi et al. 2020, for more detailed discussion). The source plane is fixed at $z_s = 1.0$. In each panel, the upper curves correspond to the all-sky $S_\ell$ estimates and the lower curves correspond to the pseudo-$\hat{S}_\ell$s (see equation 20b). One realization of the all-sky maps was considered. To simulate noise, we have included a source density ($n_s$) of 30 arcmin$^{-2}$. With *Euclid*-type noise, the error bars are nearly identical to what was presented in Fig. 2. To amplify the effect of noise, we have artificially increased the noise by a factor of 2.

(iv) *Euclid-like mask, noise, and skew spectrum:* In Fig. 12, we show the three skew spectra for a *Euclid*-like survey. We use a 'pseudo *Euclid*'' mask. To construct this mask, all pixels lying within 22 deg of either the galactic or ecliptic planes are discarded. Such a mask leaves 14 490 $\deg^2$ of the sky making, i.e. a fraction of the sky covered $f_{\rm sky} \approx 0.35$ (see Munshi et al. 2020, for more detailed discussion). We use maps with source plane fixed at $z_{\rm s} = 1.0$. In each panel, the upper curves correspond to the all-sky $S_\ell$ estimates and the lower curves correspond to the pseudo-$\hat{S}_\ell$s (see equation 20b). To compute the scatter, one realization of the map was considered. To simulate noise, we have included a source density ($n_{\rm s}$) of 30 $\rm arcmin^{-2}$. However, we found that the *Euclid*-type noise does not produce any significant effect on the scatter. To increase the effect of noise, we have artificially increased the level of noise by a factor of 2.

In Fig. 10, we plot the skew spectra related to $\langle \kappa^2_{\rm LSS}\kappa_1\rangle$ and in Fig. 11 the skew spectra corresponding to $\langle \kappa_{\rm LSS}\kappa^2_1\rangle$ are being plotted. Compared to the low-$z$ cases, the theoretical predictions for $\langle \kappa_1\kappa^2_{\rm LSS}\rangle$ are found to significantly overestimate the simulation results. This is true to a lesser extent for $\langle \kappa^2_1\kappa_{\rm LSS}\rangle$. This may be related to the fact that the simulation using a Gaussian realization at higher redshifts ($z_{\rm s} > 7.1$) may lead to the suppression of non-Gaussianity. The descrepancy becomes, however, not so significant when compared with the scatter within the beam.

## 8 CONCLUSIONS AND FUTURE PROSPECTS

The high S/N of the skew spectra and the flexibility with which they can be implemented are rather encouraging. The accuracy of the fitting function in reproducing the numerical simulations opens up several possible avenues of research.

### 8.1 Perturbative contributions from trispectrum

Beyond the leading-order non-Gaussian corrections, which come from bispectrum, the four generalized kurtosis parameters, $K^{(0)}$, $K^{(1)}$, $K^{(2)}$, and $K^{(3)}$, play an important role in perturbative reconstruction of the morphology of a non-Gaussian field. These are the contributions denoted as $\delta V^{(3)}_k$ in equation (4). These kurtosis parameters were generalized to kurtosis spectra in a manner similar to the generalization of the skewness parameters to the skew spectrum (Munshi et al. 2016). The kurtosis spectra were used in the context of CMB studies and sources of non-Gaussianity studied include the primordial non-Gaussianity as well as lensing-induced non-Gaussianity. Extension of our results to incorporate higher order terms in the context of weak lensing studies for gravity-induced non-Gaussianity will require an analytical model of the trispectrum. The analytical expression for the perturbative trispectrum is more involved and will require a dedicated study. Various other options to include the validity domain of the perturbative expression include effective field theoretic or HM-based approaches. We plan to extend our results in future in these directions.

### 8.2 Study of morphology from shear maps

In our study, we have extracted the generalized skew spectra directly from convergence maps. This requires an intermediate step of map making from shear maps. However, our method can also be generalized to directly deal with shear maps by implementing an E/B decomposition of shear maps. The PSL approach can be generalized to deal with such a decomposition and deal with arbitrary mask. This will be useful in bypassing the map-making process needed for generating convergence maps. This will also be important dealing directly with spurious magnetic or *B* mode generated due to unknown systematics. For a survey with small sky coverage, E/B decomposition may not be straightforward and one option would be to work in the real space with the correlation functions of shear. This can be achieved by a generalization of equation (18) for shear.

### 8.3 Likelihood analysis and covariance matrix

Any cosmological parameter inference using MFs would require a detailed characterization of covariance matrix of the skew spectra. The calculation of covariance matrices was presented in Munshi et al. (2011d) using a simplistic approach that is valid in the noise-dominated regime, i.e. in the limit of vanishing non-Gaussianity. This is achieved by ignoring the contributions from all higher order non-Gaussianity. While such approximate treatment may be enough to deal with present generation of surveys, stage-IV observation including the *Euclid* will map the sky with higher S/N and a more accurate modelling is thus required. A full analysis is beyond the scope of this paper. The accuracy of such an approximation will depend on the size and depth of the survey, smoothing angular scale, and the noise characteristics of rhe survey. A formal analysis will be presented as a separate paper.

### 8.4 Intrinsic allignment

The intrinsic allignment (IA) remains a major contamination to the gravity-induced secondary non-Gaussianity. Analytical modelling of IA is challenging though quite a few physically motivated models can capture certain aspects of the non-Gaussianity induced by IA (Vlah, Chisari & Schmidt 2020). Typically at the level of bispectrum, IA is expected to contribute at 10 per cent of the gravity-induced non-Gaussianity. Using the skew spectra introduced here, it will be possible to compute the corrections to the morphological change induced by IA. In addition, optimal weights combined with a match filtering approach can in effect may lead to separation of the two sources.

### 8.5 Betti number and other topological estimators

The MFs were recently generalized in a series of paper to tensorial Minkowski functionals (TMF) in 2D and 3D as well as in redshift space (Appelby et al. 2018; Chinangbam et al. 2017). The results presented here will be extended to the case of TMF for a 3D convergence map in future. Other estimators related to the morphology of cosmological fields have recently attracted attention, such as the Betti numbers (Pranav et al. 2019). Reconstruction techniques used here can be useful in these contexts.

### 8.6 Optimality and flexibility of implementation

We have not included optimal weighting in our estimator as the S/N is very high for low source redshift studies. This is not completely true for the studies involving $\kappa$ maps. Various methods can be used to improve the S/N including a Wiener or 'Wiener-like' filtering of $\kappa$ maps (Ducout et al. 2013). Alternatively, following Munshi & Heavens (2010), the generalized skew spectra can include optimal weights that inherit a match filtering approach. However, there is a price to pay as the direct links to morphology will be lost and the estimators will have less flexibility in dealing with partial sky coverage as the PSL developed in our study will not be valid.

### 8.7 Beyond λCDM matter scenarios

Though we have only discussed the gravity-induced secondary non-Gaussianity as a possible source of non-Gaussianity, many other sources of non-Gaussianities can also be included in our framework, e.g. primordial non-Gaussianity or non-Gaussianity induced by active source of perturbations or topological defects can also be studied using their impact on the morphology of convergence maps. Many modified gravity theories predict a different form of bispectrum compared to GM and their impact on morphology can be studied using the formalism developed here (Munshi & McEwen 2020).

## ACKNOWLEDGEMENTS

DM is supported by a grant from the Leverhulme Trust at MSSL. DM would like to thank Chiaki Hikage and Geraint Pratten for useful discussions during the initial phase of this project. DM would also like to thank the members of Euclid Forward Modelling Working group including Benjamin Wandelt, Adam Amara, and Martin Kilbinger for critical comments. We would like to thank Peter Taylor for providing us his code to generate the *Euclid*-type mask used in our study.

## DATA AVAILABILITY

No new data were generated in support of this research. The simulations used in this work are publicly available.

## REFERENCES

Abbott et al., 2016, Phys. Rev. D, 94, 022001
Appleby S., Chingangbam P., Park C., Hong S. E., Kim J., Ganesan V., 2018, APJ, 858, 87
Barber A. J., Munshi D., Valageas P., 2004, MNRAS, 347, 667
Bartelmann M., Schneider P., 2001, Phys. Rep., 340, 291
Bernardeau F., Colombi S., Gaztanaga E., Scoccimarro R., 2002, Phys. Rep., 367, 1
Canavezes A. et al., 1998, MNRAS, 297, 777
Castro P. G., Heavens A. F., Kitching T. D., 2005, astro-ph/0503479, PRD, 72, 2005, 023516.
Chingangbam P., Yogendran K. P., Joby P. K., Ganesan V., Appleby S., Park C., 2017, 12, 23
Clifton T., Ferreira P. G., Padilla A., Skordis C., 2012, Phys. Rep., 513, 1
Coles P., 1988, MNRAS, 234, 509
Desjacques V., Jeong D., Schmidt F., 2018, Phys. Rep., 733, 1
Drinkwater M. J. et al., 2010, MNRAS, 401, 1429
Ducout A., Bouchet F., Colombi S., Pogosyan D., Prunet S., 2013, MNRAS, 429, 2104
eBOSS Collaboration, 2021, Phys. Rev. D, 103, 083533
Eisenstein D. J. et al., 2011, AJ, 142, 72
Gil-Marín H., Wagner C., Fragkoudi F., Jimenez R., Verde L., 2012, J. Cosmol. Astropart. Phys., 02, 047
Gleser L., Nusser A., Ciardi B., Desjacques V., 2006, MNRAS, 370, 1329
Gorski K. M., Hivon E., Banday A. J., Wandelt B. D., Hansen F. K., Reinecke M., Bartelman M., 2005, ApJ, 622, 759
Gott J. R., Mao S., Park C., Lahav O., 1992, ApJ, 385, 26
Gott J. R., Mellot A. L., Dickinson M., 1986, ApJ, 306, 341
Gott J. R., Park C., Juszkiewicz R., Bies W. E., Bennett D. P., Bouchet F. R., Stebbins A., 1990, ApJ, 352, 1
Gott J. R. et al., 1989, ApJ, 340, 625
Hadwiger H., 1959, Normale Koper im Euclidschen raum und ihre Topologischen and Metrischen Eigenschaften, Math Z., 71, 124
Harnois-Déraps J., Munshi D., Valageas P., van Waerbeke L., Brax P., Coles P., Rizzo L., 2015, MNRAS, 454, 2722
Hikage C. et al., 2002, Publ. Astron. Soc. Japan, 54, 707
Hikage C., Coles P., Grossi M., Moscardini L., Dolag K., Branchini E., Matarrese S., 2008, MNRAS, 385, 1613
Hikage C., Komatsu E., Matsubara T., 2006, ApJ, 653, 11

Hikage C., Matsubara T., Coles P., Liguori M., Hansen F. K., Matarrese S., 2008, MNRAS, 389, 1439
Joyce A., Jain B., Khoury J., Trodden M., 2015, Phys. Rep., 568, 1
Kerscher M., Mecke K., Schmalzing J., Beisbart C., Buchert T., Wagner H., 2001, A&A, 373, 1
Kilbinger M., 2015, Rep. Prog. Phys., 78, 086901
Kuijken K. et al., 2015, MNRAS, 454, 3500
Laureijs R. et al., 2011, ESA/SRE(2011)12
Lesgourgues J., Pastor S., 2006, Phys.Rep., 429, 307
Mandelbaum R., 2018, ARA&A, 56, 393
Marozzi G., Fanizza G., Di Dio E., Durrer R., 2016, J. Cosmol. Astropart. Phys., 1609, 028
Matsubara T., Jain B., 2001, ApJ, 552, L89
Melott A. L., 1990, Phys. Rep., 193, 1
Moore B. et al., 1992, MNRAS, 256, 477
Munshi D., 2000, MNRAS, 318, 145
Munshi D., Heavens A., 2010, MNRAS, 401, 2406
Munshi D., Heavens A., Coles P., 2011, MNRAS, 411, 2161
Munshi D., Heavens A., Cooray A., Smidt J., Coles P., Serra P., 2011, MNRAS, 412, 1993
Munshi D., Hu B., Matsubara T., Coles P., Heavens A., 2016, J. Cosmol. Astropart. Phys., 04, 056
Munshi D., Jain B., 2000, MNRAS, 318, 109
Munshi D., Jain B., 2001, MNRAS, 322, 107
Munshi D., Kitching T., Heavens A., Coles P., 2011, MNRAS, 416, 1629
Munshi D., McEwen J. D., 2020, MNRAS, 498, 5299
Munshi D., Namikawa T., Kitching T. D., McEwen J. D., Bouchet F. B., 2020, MNRAS, 498, 6057
Munshi D., Namikawa T., Kitching T. D., McEwen J. D., Bouchet F. R., 2020a, MNRAS, 498, 6057
Munshi D., Namikawa T., Kitching T. D., McEwen J. D., Takahashi R., Bouchet F. R., Taruya A., Bose B., 2020, MNRAS, 493, 3985
Munshi D., Valageas P., Barber A. J., 2004, MNRAS, 350, 77
Munshi D., Valageas P., van Waerbeke L., Heavens A., 2008, Phys. Rep., 462, 67
Munshi D., Smidt J., Heavens A., Coles P., Cooray A., 2011, MNRAS, 411, 2241
Munshi D., Smidt J., Joudaki S., Coles P., 2012, MNRAS, 419, 138
Munshi D., van Waerbeke L., Smidt J., Coles P., 2012, MNRAS, 419, 536
Namikawa T., Bose B., Bouchet F. R., Takahashi R., Taruya A., 2019, Phys. Rev. D, 99, 063511
National Research Council, 2010, New Worlds, New Horizons in Astronomy and Astrophysics. Natl. Acad. Press
Natoli P. et al., 2010, MNRAS, 408, 1658
Novikov D., Schmalzing J., Mukhanov V. F., 2000, A&A, 364, 17
Park C. et al., 2005, ApJ, 633, 11
Petri A., Haiman Z., Hui L., May M., Kratochvil J. M., 2013, Phys. Rev. D, 88, 123002
Planck Collaboration XVI, 2014, A&A, 571, A16
Planck Collaboration XVII, 2016a, A&A, 594, A17
Planck Collaboration XIII, 2016b, A&A, 594, A13
Planck Collaboration IX, 2020a, A&A, 641, A9
Planck Collaboration VI, 2020b, A&A, 641, A6
Pranav P. et al., 2019, MNRAS, 485, 4167
Pratten G., Lewis A., 2016, J. Cosmol. Astropart. Phys., 08, 047
Sato J., Takada M., Jing Y. P., Futamase T., 2001, ApJ, 551, L5
Schmalzing J., Diaferio A., 2000, MNRAS, 312, 638
Schmalzing J., Górski K. M., 1998, MNRAS, 297, 355
Scoccimarro R., Frieman J. A., 1999, ApJ, 520, 35
Takahashi R., Hamana T., Shirasaki M., Namikawa T., Nishimichi T., Osato K., Shiroyama K., 2017, ApJ, 850, 23
Taruya A., Takada M., Hamana T., Kayo I., Futamase T., 2002, ApJ, 571, 638
Tomita H., 1986, Prog. Theor. Phys., 76, 952
Tyson J. A., Wittman D. M., Hennawi J. F., Spergel D. N., 2003, Nucl. Phys. B, 124, 21
Valageas P., Barber A. J., Munshi D., 2004, MNRAS, 347, 654
Valageas P., Munshi D., Barber A. J., 2005, MNRAS, 356, 386
Vlah Z., Chisari N. E., Schmidt F., 2020, JCAP, 1, 25
Weiss A. J., Schneider A., Sgier R., Kacprzak T., Amara A., Refregier A., 2019, JCAP, 10, 11

This paper has been typeset from a TEX/LATEX file prepared by the author.